Rare Met. (2022) 41(2):546–558
https://doi.org/10.1007/s12598-021-01852-8

RARE METALS

ORIGINAL ARTICLE

Atomic layer deposition of zinc oxide onto 3D porous iron scaffolds for bone repair: in vitro degradation, antibacterial activity and cytocompatibility evaluation

Yu-Lei Li, Jin He, Hai-Xia Ye, Can-Can Zhao, Wei-Wei Zhu, Xiong Lu, Fu-Zeng Ren*

Received: 22 May 2021 / Revised: 4 July 2021 / Accepted: 9 July 2021 / Published online: 22 November 2021

Abstract 3D porous iron (Fe) scaffolds with interconnected open pores are promising candidates for bone repair. However, the bare 3D porous Fe scaffolds lack of antibacterial activity and the ability for cell adhesion. Herein, atomic layer deposition technique was used to deposit nanometer-thick zinc oxide (ZnO) layer onto the skeleton of 3D porous Fe scaffolds with interconnected open pores. The effect of ZnO thin film on the in vitro degradation behavior, antibacterial activity and cytocompatibility of 3D porous Fe scaffolds was systematically evaluated. The results showed that a dense ZnO thin film with a thickness of 76 nm was uniformly deposited on the skeleton of the porous Fe scaffolds. The thickness of ZnO thin film could be easily controlled by the deposition cycles. The deposited ZnO thin film significantly reduced the degradation rate of porous Fe scaffolds and the fabricated ZnO coated porous Fe scaffolds demonstrated strong antibacterial ability against both Gram-negative *Escherichia coli* and Gram-positive *Staphylococcus aureus*, while did not significantly affect cytocompatibility and could also promote cell adhesion.

Keywords Atomic layer deposition; Porous iron scaffolds; ZnO; Antibacterial activity

1 Introduction

Iron (Fe) and its based alloys have recently attracted much interest due to their adequate mechanical properties and biodegradable characteristics, and considerable research efforts have been devoted to the design and development of Fe-based biodegradable vascular stents and bone scaffolds [1–5]. In particular, three-dimensional (3D) porous Fe scaffolds with interconnected micropores have emerged as a promising candidate for bone repair and regeneration [6–11], since they can not only increase the degradation rate and reduce the modulus of metallic alloys, but also facilitate ions exchange, allow the ingrowth of the new tissue and promote the repair of the defect [12].

For clinical use of biodegradable Fe scaffolds, there are several critical issues to be solved. First, the slow degradation rate and high elastic modulus of the bulk Fe scaffolds can be solved by fabricating the scaffold into 3D porous form [5, 13, 14]. However, for the porous Fe scaffolds, the fast degradation and high concentration of released Fe ions could cause cytotoxicity [9, 15–17]. To improve the biocompatibility of the porous Fe scaffolds, various coating strategies have been developed. These coatings include inorganic calcium phosphates [15, 18–22], polymeric materials [23, 24] and the inorganic-organic composites [25]. Last but not least, as an implant, the porous Fe scaffolds are lack of antibacterial activity. The

Supplementary Information The online version contains supplementary material available at https://doi.org/10.1007/s12598-021-01852-8.

Y.-L. Li, J. He, H.-X. Ye, C.-C. Zhao, W.-W. Zhu, F.-Z. Ren*
Department of Materials Science and Engineering, Southern University of Science and Technology, Shenzhen 518055, China
e-mail: renfz@sustech.edu.cn

W.-W. Zhu
Institute of Applied Physics and Materials Engineering, Faculty of Science and Technology, University of Macau, Macau 999078, China

X. Lu
Key Lab of Advanced Technologies of Materials, Ministry of Education, School of Materials Science and Engineering, Southwest Jiaotong University, Chengdu 610031, China

possibility of bacterial adhesion to the implant surface and subsequent biofilm formation at the implantation site may cause resistant chronic infection or tissue necrosis [26, 27]. Implant-associated infections are extremely resistant to antibiotics and host defenses and frequently persist until the implant is removed. In order to inhibit bacterial adhesion and diminish infection, antibacterial surface coating by incorporating antimicrobial agents offers a promising strategy [28, 29]. These antibacterial coatings should have sustainable antibacterial effects and avoid the burst release of antimicrobial agents which may cause biosafety concerns.

Zinc oxide (ZnO) has been reported to have a broad-spectrum of antibacterial activity [30–32] and frequently used as antibacterial agent in biomedical field [33–36]. Moreover, the released Zn ions play an important role in bone regeneration, which could stimulate bone formation and accelerate mineralization [37, 38]. Therefore, depositing nanometer-thick ZnO layer onto porous Fe scaffolds may reduce degradation rate and increase the antibacterial properties. However, it is a grand challenge to coat a uniform ZnO thin film on the skeleton of the porous Fe scaffolds due to the shape complexity, especially inside the scaffolds.

Atomic layer deposition (ALD) is a chemical vapor deposition system and has frequently been used to synthesize high-quality metal oxide thin films for electronic devices [39, 40]. The ALD system can allow the gaseous reactants to go through the interconnected pores and deposit products on internal surface. Thus, the entire skeleton surface can be coated with a uniform ZnO nanometer-thick layer.

In this context, we first fabricated the 3D porous Fe scaffolds with interconnected open micropores using a template-assisted electrochemical deposition method. Then, ALD was used to deposit a uniform nanometer-thick ZnO layer on the skeleton of 3D porous Fe scaffolds (ZnO@Fe). Based on a detailed characterization of ZnO@Fe scaffolds, we systematically evaluated the effect of ZnO coating on the in vitro degradation behavior, antibacterial activity and cytocompatibility.

2 Materials and methods

2.1 Fabrication of 3D porous ZnO@Fe scaffolds

The 3D porous Fe scaffolds were fabricated via a facile template-assisted electrodeposition method, as detailed in our previous work [19]. Briefly, open-cell polyurethane (PU) foams coated with conductive colloidal graphite were used as the templates. A ferrous chloride solution ($FeCl_2{\cdot}4H_2O$) with pH 2.5 was used as the electrolyte. Conductive PU foams and two pure Fe sheets were used as the cathodes and the double anodes, respectively. Electrodeposition was performed at a current density of 0.06 $A{\cdot}cm^{-2}$ for 2 h using a direct current (DC) power supply, during which the temperature was maintained at 50 °C by a water bath. The template was then removed after heat-treated at 550 °C for 1 h and 950 °C for another 1 h in a tube furnace with a constant flow (f) of nitrogen-hydrogen mix gas ($f(N_2)$:$f(H_2)$ = 8:1).

The porous Fe scaffolds were cut into disks with a dimension of Φ10 mm × 3 mm using electrical discharge machining. In order to remove the oxides and contaminants on the skeleton surface of as-fabricated scaffolds and obtain a uniform and smooth ZnO thin film, porous Fe scaffolds were ultrasonically cleaned with acid solution (a mixture of 10 vol% HCl and 10 vol% H_2SO_4), ethanol and deionized water sequentially and dried in a vacuum oven (SalvisLAB, VC 20, Swiss) at 60 °C for 2 h.

The deposition of ZnO thin film was carried out in a Picosun R-200 ALD system (Picosun Oy, Finland) with a working base pressure of 600 Pa. Diethylzinc ($Zn(C_2H_5)_2$, DEZn; 99.98%; Valley Gas Co., Ltd., Shenzhen, China) and deionized water were used as the precursors for the deposition of ZnO. High purity nitrogen gas (99.9999%) was used as carrier and purge gas in each cycle. A schematic illustration of the process of atomic layer deposited ZnO thin film on 3D porous Fe scaffolds is presented in Fig. 1. Optimized processing parameters including carrier gas flow, plus and purge time for deposition of ZnO thin film were listed in Table 1. The deposition temperature was set at 200 °C, and the typical growth rate was 0.19 nm per cycle by using DEZn and H_2O [40].

The chemical reaction in the process can be summarized in the following equation:

$$Zn(CH_3CH_2)_2(g) + H_2O(g) \xrightarrow{200\ ^\circ C} ZnO(s) + 2C_2H_3(g) \quad (1)$$

2.2 Material characterization

The surface morphology and composition of the deposited thin film were characterized by a field emission scanning electron microscope (FESEM, Tescan MIRA3, Czech Republic) equipped with energy dispersive X-ray spectroscopy (EDX, AZtec EDX system with an X-Max^N 50 mm^2 silicon drift detector, Oxford Instruments, UK). The thickness of ZnO film was confirmed by a focus ion beam system (FIB, Helios Nanolab^{TM} 600i, FEI, USA). The phases of the coated and bare Fe scaffolds were identified by X-ray diffraction (XRD) recorded by a diffractometer (Rigaku Smartlab-9 kW, Japan) in the 2θ range from 30° to 55° using a Cu Kα (λ = 0.15406 nm, 45 kV, 200 mA) as the radiation source.

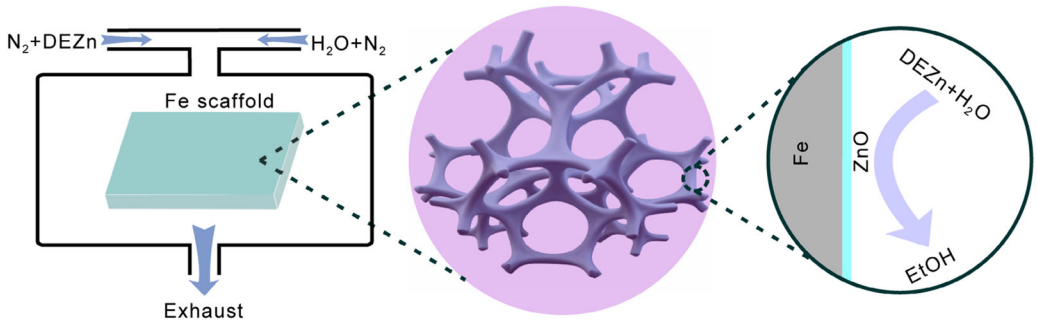

Fig. 1 Schematic illustration of process of atomic layer deposited ZnO coating on 3D porous Fe scaffolds

Table 1 ALD process parameters for ZnO thin film

Reactants	Carrier gas flow/(ml·min^{-1})	Plus time/s	Purge time/s
DEZn	150	0.1	4
H_2O	200	0.2	4

2.3 In vitro biodegradation tests and ions release

The effect of ZnO thin film on degradation behavior of porous Fe scaffolds was studied by static immersion tests according to ASTM NACE TM0169/G31-12a (2012). The two groups of scaffolds (bare porous Fe scaffolds and ZnO@Fe) with size of Φ5 mm × 3 mm were weighted before immersed in 3 ml Hank's solution [41] in centrifuge tubes and the centrifuge tubes were kept in a shaking water bath (Memert WNE 14, Germany) at 37 °C for 28 days. At each predefined time point (7, 14, 21 and 28 days), the pH values of solutions were measured. After immersion, the scaffolds were gently rinsed with ethanol and dried in a vacuum oven at 60 °C for 2 h. Then, the corrosion morphology and products were examined by SEM and EDX. After removing the degradation products from the skeleton surface by immersion in a 10 mol·L^{-1} NaOH solution according to the standard of ASTM G1-03(2017)^{e1}, the scaffolds were weighted again. The weight loss (W_L) percentages were then calculated using the following equation:

$$W_L = (W_o - W_i)/W_o \times 100\% \quad (2)$$

where W_o and W_i were the original weight and the weight after immersion in Hank's solution for the predefined times and removing degradation products, respectively.

The amounts of Fe and Zn ions released from scaffolds in Hank's solution for 28 days were measured by inductively coupled plasma mass spectrometry (IPC-MS, Agilent 7700x, USA). At each time point, 1 ml solution was collected for ICP-MS analysis and 1 ml fresh Hank's solution was added to keep the sample/solution volume ratio a constant.

2.4 Antibacterial activity assay

The antibacterial activity of ZnO thin film was investigated using spread plate method. Both Gram-negative *Escherichia coli* (*E. coli*, ATCC 25922) and Gram-positive *Staphylococcus aureus* (*S. aureus*, ATCC 29231) of standard strains were used. Luria-Bertani (LB) culture medium and the agar plates were sterilized by autoclaving at 121 °C for 15 min. The samples were first sterilized by 75% ethanol and rinsed with sterilized phosphate-buffered saline (PBS, HyClone^{TM}, USA) three times, then were transferred into a 48-well plate (Costar®, NY, USA). Each well was added with 400 ml diluted bacterial suspension (1×10^6 CFU·ml^{-1}, where CFU represents colony-forming unit). After 24 h incubation at 37 °C in an incubator, the bacterial suspension in each well was transferred to a sterilized tube. Each sample was washed by sterilized PBS three times to collect the bacteria on scaffolds. Then, the bacterial suspension was diluted tenfold by sterilized PBS, and 100 μl diluted suspension was dropped and spread on LB agar plates, and the agar plates were incubated at 37 °C for another 24 h. Finally, the number of colonies on each agar plate was counted. The antibacterial rate of ZnO@Fe scaffolds was calculated by the following formula:

$$\text{Antibacterial rate} = \frac{CFU_{Fe} - CFU_{ZnO@Fe}}{CFU_{Fe}} \times 100\% \quad (3)$$

where CFU_{Fe} and $CFU_{ZnO@Fe}$ represent the numbers of CFUs of porous Fe and ZnO@Fe scaffolds, respectively.

The bacterial morphology was observed by SEM. The bacteria on the samples were fixed with 4% paraformaldehyde for 30 min at room temperature, dehydrated in a series of ethanol, freeze-dried and sputter-coated with platinum for SEM observation.

2.5 In vitro cytotoxicity evaluation

2.5.1 Osteoblast proliferation by MTT assay

The effect of ZnO thin film on cytotoxicity of porous Fe scaffolds was evaluated using the extraction method according to ISO 10993-5:2009(E). Mouse calvaria pre-osteoblasts, known as MC3T3-E1 (subclone 14) cells, were purchased from the Cell Bank of the Chinese Academy of Sciences (Shanghai, China). MC3T3-E1 pre-osteoblasts were cultured in alpha minimum essential medium (α-MEM, Gibco®, USA) containing 10 vol% fetal bovine serum (FBS; Hyclone) and 1 vol% streptomycin-penicillin (Antibiotic-Antimycotic, Hyclone, USA) in a humidified atmosphere of 95% air and 5% CO_2 at 37 °C. The extracts of scaffolds were prepared in accordance with the standard ISO 10993-12:2012. The two groups of scaffolds were first ultrasonically cleaned in ethanol and distilled water, respectively, and then sterilized by ultraviolet irradiation and immersion in 75% ethanol. After washed with sterile PBS and serum-free α-MEM, the sterilized scaffolds were then immersed in α-MEM for 24 h in the cell incubator. The ratio of volume of medium and weight of scaffold was set as 0.2 g·ml^{-1}. The collected α-MEM was centrifuged and supplemented with 10 vol% FBS and 1 vol% mixed solution of penicillin and streptomycin.

The cells were seeded in 96-well plates with a density of 1×10^4 cells per well. After a pre-culture for 24 h in 100 μl complete α-MEM, culture media were replaced with complete α-MEM, extracts, and α-MEM with 10 vol% dimethyl sulfoxide (DMSO) which was negative, test and positive group, respectively. After incubation for 1, 2 and 4 days, the culture media were replaced with serum-free α-MEM at each time point, following by adding 10 μl (5 mg·ml^{-1}) MTT solution (Solarbio, China). After another 4 h incubation, the media were removed and a volume of 150 μl DMSO was added to each well to dissolve the formazan crystals, then optical density (OD) of each well was measured using a multi-mode microplate reader (Biotek, Cytation 3) at the wavelength of 570 nm and the reference wavelength of 630 nm, respectively.

2.5.2 Immunofluorescence staining

The cytoskeletal filamentous actin (F-actin) and nuclei were also stained for fluorescence microscopy observation. The cells on scaffolds after 1 day of incubation were gently rinsed by PBS and fixed in 4% paraformaldehyde for 15 min at room temperature, followed by an immersion in 0.1% Triton X solution for another 15 min. Then the cells were blocked in 3% bovine serum albumin (BSA) for 30 min. 10 mg·ml^{-1} Alexa Fluor^{TM} 568 Phalloidin (Thermo Fisher Scientific^{TM}, A12380, USA) in PBS solution containing 3% BSA was used to stain actin filaments, and 1 mg·ml^{-1} Hoechst 33258 was used to stain cell nuclei. After washing with PBS, the cells were observed by a fluorescence microscope (Zeiss Axio Observer Z1, Germany).

2.6 Statistical analysis

All data in the present work were expressed as means ± standard deviations (SD) of at least three independent experiments. A one-way ANOVA was conducted and a statistical significance was defined as $*p < 0.05$ and $**p < 0.01$.

3 Results

3.1 Characterization of scaffolds

The phase of the deposited thin film was confirmed by XRD (Fig. 2). In comparison with the bare porous Fe scaffolds, three additional reflections at $2\theta = 31.7°$, 34.4° and 36.2°, which were assigned to be (100), (200) and (101) of ZnO, respectively, were also observed in XRD pattern of the ZnO@Fe scaffolds. The deposited ZnO had a wurtzite structure (JCPDS No.36-1451).

Figure 3 shows a comparison of the morphology between the bare porous Fe and ZnO@Fe scaffolds. The as-fabricated Fe scaffolds have a highly 3D porous structure (porosity of 91%) with an average pore size of (345 ± 82) μm and skeleton diameter of (143 ± 16) μm. Such 3D porous structure with interconnected pores would facilitate transport of nutrients and metabolic waste, allow the ingrowth of the new tissue and promote the repair of bone defects. After 600-cycles ALD-ZnO deposition, the color of porous Fe scaffolds changed from brown to light violet. The color change could be attributed to nanometer size effect of the ZnO thin film (note that the direct

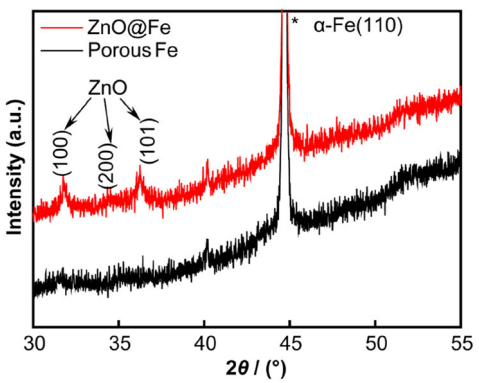

Fig. 2 XRD patterns of porous Fe and ZnO@Fe scaffolds

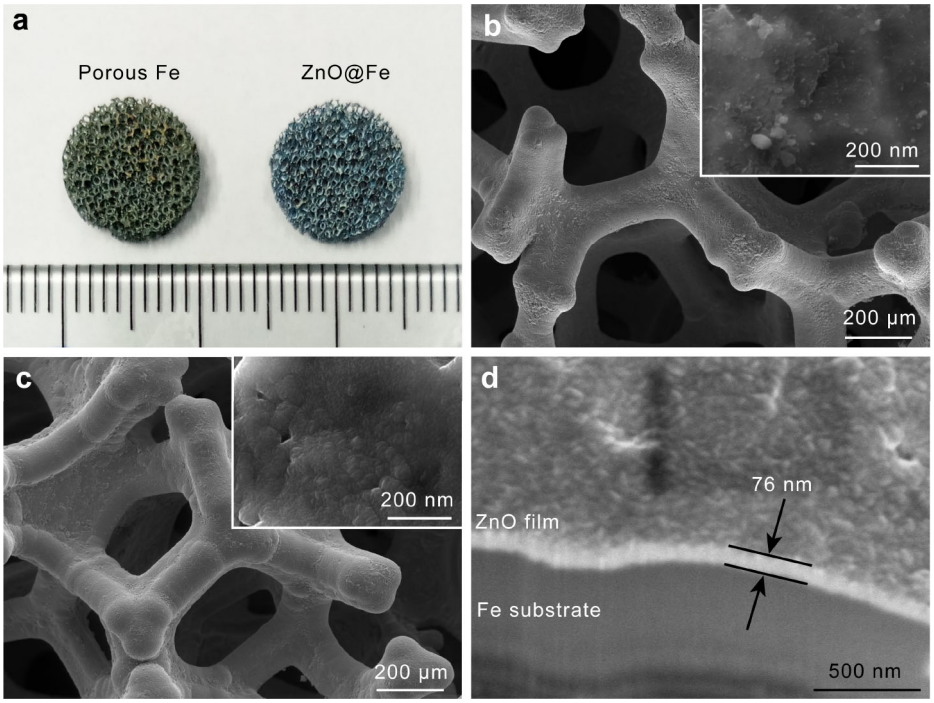

Fig. 3 Morphology of 3D porous Fe and ZnO@Fe scaffolds: **a** photograph showing distinct appearance of original 3D porous Fe and ZnO@Fe scaffolds; SEM images of **b** porous Fe and **c** ZnO@Fe scaffolds and (insets) images with higher magnifications; **d** secondary electron image of FIB-milled cross section of the skeleton of ZnO@Fe scaffold

bandgap (E_g) of ZnO is ~ 3.3 eV). SEM images further revealed that the deposited thin film consisted of dense equiaxed ZnO nanoparticles, uniformly covering the skeletons of the porous Fe scaffolds. FIB-milled cross section showed that the ZnO thin film was tightly bonded to the skeleton substrate with a thickness of ~ 76 nm. Such nanometer-thick thin film could still maintain the 3D interconnectivity of the porous scaffold.

The chemical composition and elemental distribution of the as-deposited scaffolds were further examined by EDX. As presented in Fig. 4, besides the iron substrate, both zinc and oxygen elements showed uniform and continuous distributions on the skeletons, indicating that the deposited ZnO thin film was uniform.

3.2 In vitro degradation and ions release

The effect of ZnO thin film on degradation behavior of bare porous Fe scaffolds was investigated by immersion tests in Hank's solution. Figure 5 shows the morphology of the two groups of porous scaffolds after immersion in Hank's solution for 7, 14, 21 and 28 days, respectively. The bare porous Fe scaffolds showed severe corrosion. After 7 days, a mass of degradation products was observed, forming a loose layer on the skeleton surface (Fig. 5a). With the increase of immersion time, the corrosion became much severer. After 28 days, the skeleton of bare porous Fe scaffolds was covered with large agglomerates of corrosion products. In the higher magnification images (insets in Fig. 5a–d), the precipitates layer consisted of a large amount of spherical particles with size of several microns. The precipitates layer showed weak adherence to the iron surface, and cracks and peeling off were observed on the surface. EDX analysis on the loose precipitates layer after immersion for 28 days showed that this layer mainly consisted of O, P, Fe and Ca, indicating the formation of phosphates on the iron surface (Fig. S1a–c). On the contrary, ZnO@Fe scaffolds showed only a slight change in structure and morphology even after 28 days immersion (Fig. 5h). High magnification SEM images showed that a small amount of spherical precipitates was located on the dense and uniform ZnO coating. EDX analysis confirmed that these spherical particles were composed of Zn, Fe, O, P and Ca, implying that these particles were phosphates (Fig. S1e). This means that the deposited ZnO nanothick coating significantly reduced the corrosion rate of the porous Fe scaffolds.

W_L was a direct index to assess the extent of degradation of materials. The W_L of bare porous Fe scaffolds was 2.99% ± 0.44% after immersion for 7 days and 9.86% ± 1.82% after 28 days (Fig. 6a), indicating fast degradation. However, after coated with a 76 nm-thick ZnO layer, the W_L of ZnO@Fe scaffolds showed negative values even after 21 days, suggesting weight gain after

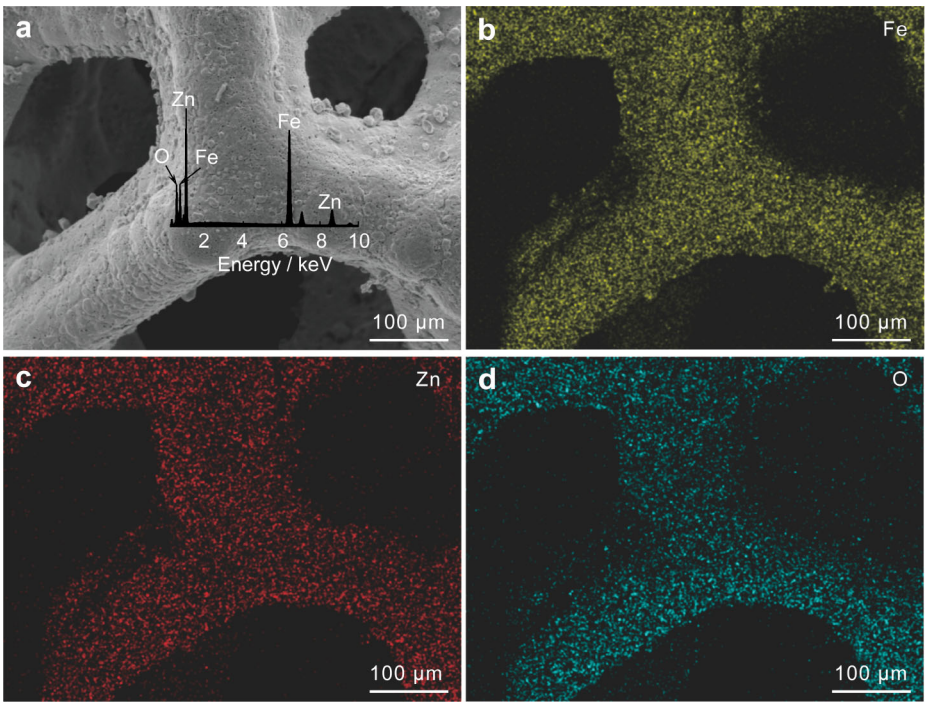

Fig. 4 Composition analysis of ZnO@Fe scaffold: **a** SEM image of skeleton of ZnO@Fe scaffold and (inset) representative EDX spectrum; **b–d** corresponding EDX elemental maps of Fe, Zn and O, respectively

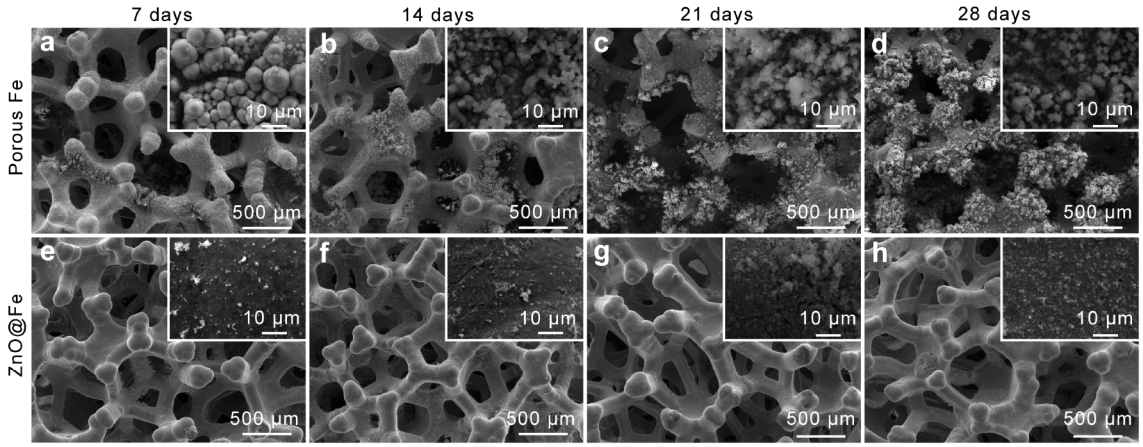

Fig. 5 Comparison of surface morphology (SEM images) of **a**, **b**, **c**, **d** porous Fe and **e**, **f**, **g**, **h** ZnO@Fe scaffolds after immersion for predefined time intervals and (insets) images with higher magnification

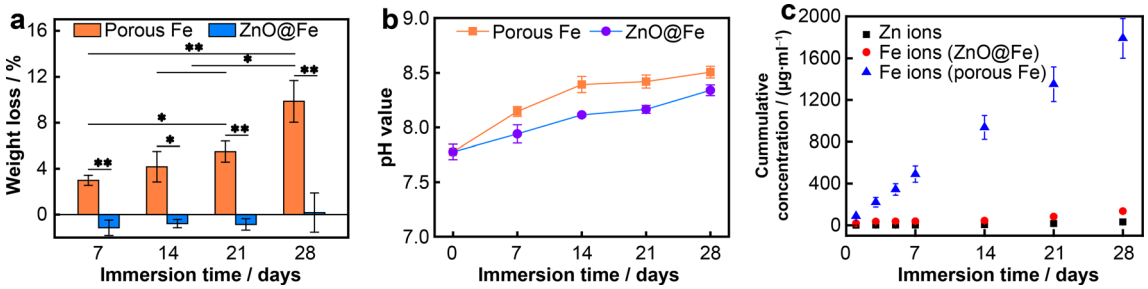

Fig. 6 **a** Weight loss, **b** evolution of pH in the solution and **c** ions release profiles with varying immersion time ($n = 3$, $^{*}p < 0.05$, $^{**}p < 0.01$)

immersion. The measured pH values of the Hank's solutions steadily increased with immersion time for both group of samples and the solutions with bare porous Fe scaffolds showed higher values which increased from 7.77 ± 0.07 to 8.51 ± 0.05 after 28 days (Fig. 6b).

The cumulative concentrations of released ions from the scaffolds during immersion were measured by ICP-MS. As shown in Fig. 6c, in the bare porous Fe scaffolds group, the cumulative concentration of the released Fe ions linearly increased with the immersion time, from (88.00 ± 5.76) $mg{\cdot}L^{-1}$ at the first day to (1789.00 ± 189.11) $mg{\cdot}L^{-1}$ at the twenty-eighth day, which indicated the rapid degradation of iron. However, after deposited with ZnO film, the released Fe ions were dramatically decreased, only (135 ± 14.69) $mg{\cdot}L^{-1}$ at the twenty-eighth day ($\sim$ 4.8 $mg{\cdot}L^{-1}{\cdot}day^{-1}$), which suggested that the coated ZnO thin film significantly reduced the degradation rate of bare porous Fe scaffolds. In addition, the release of Zn ions was also observed, despited at a low level during the immersion period. The average released concentration of Zn ions was about 1.9 $mg{\cdot}L^{-1}{\cdot}day^{-1}$ in Hank' solution, which was much lower than the recommended upper limit for the daily intake of zinc [42].

3.3 Antibacterial activity

Figure 7 shows the typical photographs of agar media with bacterial colonies and the corresponding numbers of CFUs after 24 h incubation with bare porous Fe scaffolds and ZnO@Fe. After incubation with bare porous Fe scaffolds, the numbers of *E. coli* and *S. aureus* bacteria were (44.08 ± 5.97) × 10^5 and (168 ± 41.48) × 10^5 CFUs per piece, respectively. In comparison, the numbers of *E. coli* and *S. aureus* bacteria reduced to (5.74 ± 1.18) × 10^5 and (19.47 ± 6.32) × 10^5 CFU per piece in ZnO@Fe group, respectively. The calculated antibacterial rates were 87.0% and 88.4% against *E. coli* and *S. aureus*, respectively. These results indicate that after deposition of ZnO nanolayer, the antibacterial ability of iron scaffolds is significantly enhanced against both Gram-negative and positive bacteria.

To reveal the antibacterial mechanism, the morphology of the bacteria adhered to the skeletons of the scaffolds was observed by SEM, as shown in Fig. 8. After 24 h incubation with porous Fe scaffolds, many *E. coli* cells adhered to the skeleton of the bare porous Fe scaffolds, showing typical rod-shaped appearance. Under higher magnification, the well-developed bacterial cell structure was observed. On the contrary, a much smaller number of *E. coli* cells were found on the ZnO@Fe scaffolds, and the bacterial cells were withered and even lysed, as marked with dashed circles. A similar phenomenon was also found for *S. aureus*. The round-shaped *S. aureus* cells grew well on the bare porous Fe scaffolds, however, the bacterial cells were distorted and collapsed on the ZnO@Fe porous scaffolds.

3.4 In vitro cytotoxicity

Given that the atomic layer deposited ZnO thin film can significantly increase the antibacterial activity of porous Fe scaffolds, the cytotoxicity should also be evaluated. The proliferation of MC3T3-E1 cells in 100%, 75% and 50% extracts after 1, 2 and 4 days incubation is presented in Fig. 9. Even though the cell viability at the first day is 96% in extract of porous Fe scaffolds, 100% extracts of both porous Fe and ZnO@Fe scaffolds show strong cytotoxicity to MC3T3-E1 cells (Fig. 9a). When diluted to 75% with α-MEM, extracts of porous Fe scaffolds present no cytotoxicity; however, extracts of ZnO@Fe scaffolds still hold tough cytotoxicity (Fig. 9b). When further diluted to 50% with α-MEM, the cytotoxicity of both groups' extracts is significantly reversed. Both porous Fe and ZnO@Fe scaffolds become cytocompatibility under this condition. At the fourth day, ZnO@Fe even performs better than porous Fe scaffolds (Fig. 9c). These results give evidence that the viability of MC3T3-E1 cells has a strong correlation with the concentrations of extracts, meaning that diluting extracts could decrease the cytotoxicity of both porous Fe and ZnO@Fe scaffolds, and ZnO@Fe has better cytocompatibility than porous Fe scaffolds when diluted to a certain concentration.

The cell adhesion on scaffolds was also observed by fluorescent microscope after 24 h incubation, as shown in Fig. 10. No cells were found on bare porous Fe scaffolds. This is probably due to the fast degradation of porous Fe which is not suitable for cell attachment. In contrast, a considerable number of cells were found on ZnO@Fe scaffolds. Both nuclei and the F-actin could be clearly observed (Fig. 10c, d). However, MC3T3-E1 cells did not grow and spread well, presenting in round shape, not the typical elongated morphology [43]. Similar morphology was also observed in previous studies [44, 45], probably caused by free Zn ions in culture medium. These results suggest that the deposited ZnO thin film could promote the cell adhesion on porous Fe scaffolds.

4 Discussion

Iron is an essential trace element for human bodies and plays a significant role in bone metabolism. In addition, Fe-based alloys show excellent mechanical properties and slow degradation rate, which offer sufficient mechanical support and prolonged maintenance for new bone ingrowth [10]. However, the slow degradation rate delays the bone

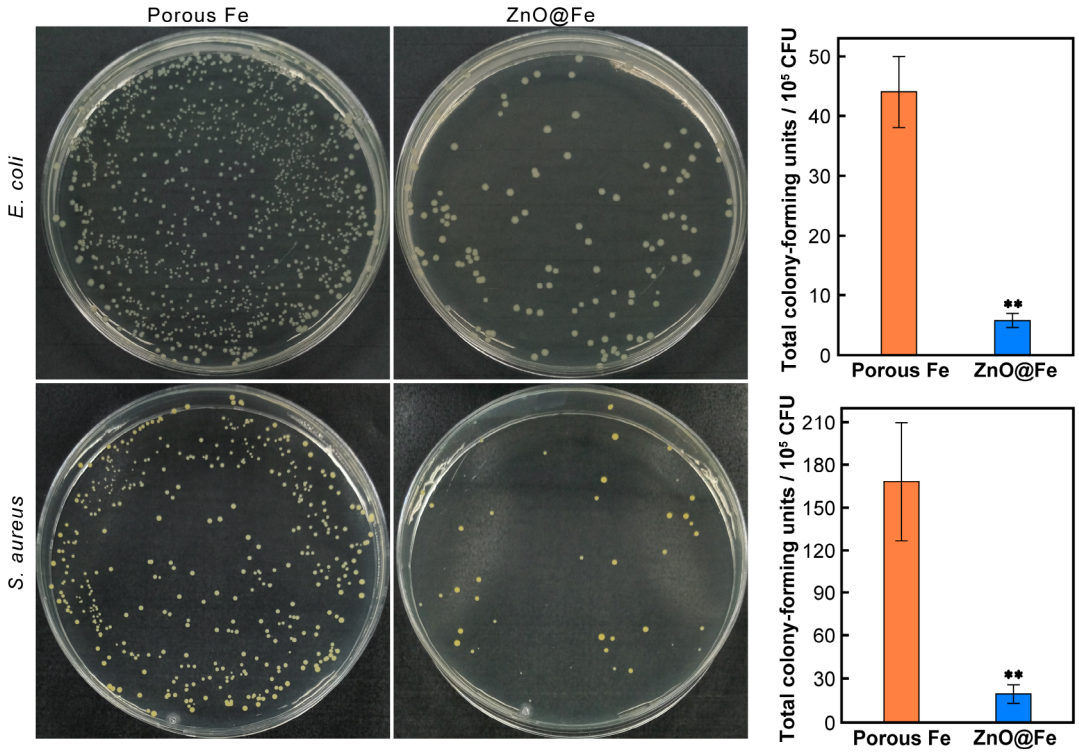

Fig. 7 Representative photographs of colonies of *E. coli* and *S. aureus* on porous Fe and ZnO@Fe scaffolds and statistical analysis of total colony-forming units (CFU/piece) (n = 3, $^{**}p < 0.01$) after 24 h incubation

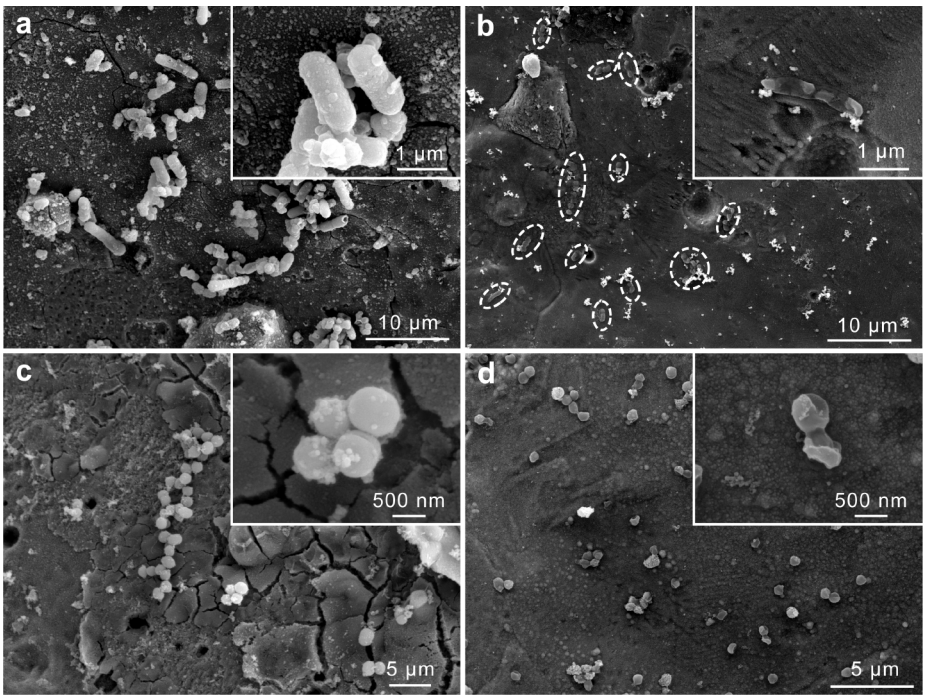

Fig. 8 SEM images and (insets) higher magnificated images of *E. coli* and *S. aureus* after 24 h incubation with scaffolds: *E. coli* on **a** porous Fe and **b** ZnO@Fe scaffolds (dotted circles in **b** marking apoptotic *E. coli* cells); *S. aureus* on **c** porous Fe and **d** ZnO@Fe scaffolds

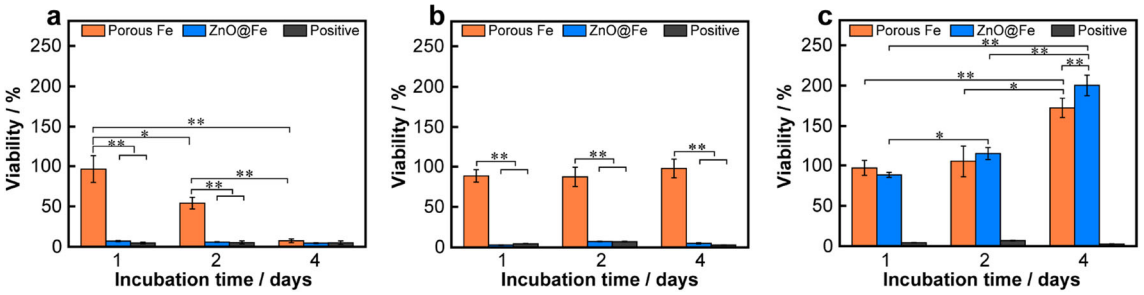

Fig. 9 MC3T3-E1 cells proliferation on porous Fe and ZnO@Fe scaffolds: **a** 100% extraction medium; **b** 75% extraction medium; **c** 50% extraction medium ($n = 3$, $^{*}p < 0.05$, $^{**}p < 0.01$)

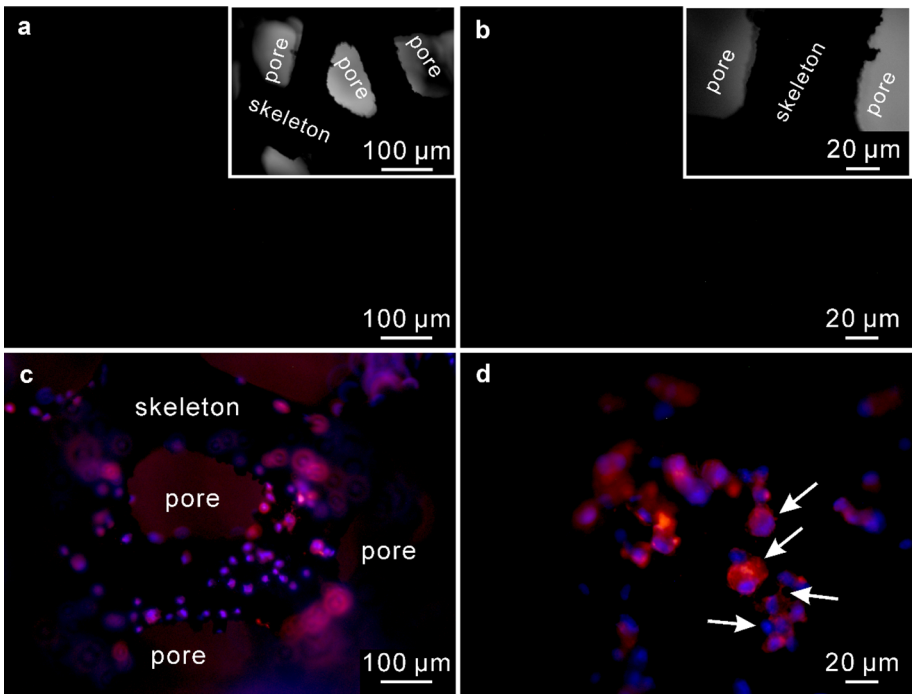

Fig. 10 Fluorescent images and higher magnificated images of MC3T3-E1 cells adhered to skeletons of **a, b** porous Fe (the insets are corresponding ones captured in bright field) and **c, d** ZnO@Fe scaffolds after 1 day of incubation

healing period. Moreover, the intrinsic lack of antibacterial properties could induce peri-implant inflammation reaction due to the bacterial infection introduced during surgical operations, which directly leads to the orthopedic implant failure. Given the above-mentioned challenges, in the present work, we have fabricated the Fe scaffolds in 3D porous form to accelerate the degradation and then coated nanometer-thick ZnO film using ALD on the skeleton surface of the porous Fe scaffolds to prevent the formation of biofilm. The obtained ZnO@Fe scaffolds show strong antibacterial ability, and could promote cell adhesion without sacrificing biocompatibility.

Distinct from the flat substrates with regular shape, the 3D interconnected open pore structure of the scaffolds poses a grand challenge to uniform coating which is in great demand for surgical applications. In terms of fabricating ZnO films or coatings, many techniques have been used including sol-gel technique [46], reactive radio frequency magnetron sputtering [35], hydrothermal synthesis [47, 48] and ALD [49]. Sol-gel technique includes two steps: (i) ZnO nanoparticles synthesis and (ii) spin coating, thus it only works for coating ZnO on plates or other regular specimens. Although ZnO films prepared by magnetron sputtering are dense, uniform and adherent to substrates, they cannot coat internal surface of porous scaffolds due to the shadow effect. Regarding to the nature of liquid phase reactions, ZnO coatings can be synthesized on the internal surface of porous scaffolds. However, the obtained coatings always show loose structure and weak bonding to the substrate. The ZnO synthesized by

hydrothermal method is often in the rod shape with high aspect ratios and in the micrometer-scale thickness [47], which can easily be peeled off from the skeletons surface during surgical operations. ALD is an advanced film fabrication technique which can precisely control thin film at the Angstrom or monolayer level. The obtained thin film is smooth and pinhole-free due to the nature of sequential, self-limiting surface reactions. Moreover, the feature of gas phase reactions extends the applications of ALD to the substrates in complex shape. Thus, it is suitable for depositing high quality ZnO thin films with nanometer-scale thickness on the 3D porous Fe scaffolds. In this work, dense, uniform and well-adhered ZnO thin film with a thickness of below 100 nm were successfully deposited on the skeleton surface of porous Fe scaffolds, and the connectivity and open pore structure were well reserved.

The degradation in physiological environment is a critical factor to the performance of metallic implants. During degradation, the metallic implants would release ions or particles into local environment which would affect biocompatibility. In addition, too fast degradation of porous biodegradable metals could also lead to mechanical failure. In this study, the bare iron scaffolds show severe corrosion after 28 days in Hank's solution, which was also demonstrated in other studies [9, 18]. The mechanism of corrosion of iron is known as localized corrosion [9, 50]. The corrosion products after 28 days was identified to be mainly γ-Fe_2O_3 (Fig. S2). The corrosion process is summarized as Eqs. (4, 5):

$$2Fe + 2H_2O + O_2 \rightarrow 2FeO{\cdot}H_2O \quad (4)$$

$$4FeO{\cdot}H_2O + O_2 \rightarrow 2Fe_2O_3 + 4H_2O \quad (5)$$

However, after deposition of nanometer-thick ZnO, the degradation rate was apparently reduced, as demonstrated by both ICP-MS analysis and the increasing pH. As is well known, ZnO is a typical amphoteric oxide which can react with H^+ as well as OH^- and release Zn ions to the solution. Previous studies have demonstrated that slow release of Zn ions could enhance the alkaline phosphatase (ALP) activity, extracellular matrix (ECM) mineralization and osteogenic related genes or proteins expression [38, 51]. However, rapid release of Zn ions has negative effect on the cellular growth and proliferation [52]. In this study, the release of Zn ions is only 1.9 $mg{\cdot}L^{-1}{\cdot}day^{-1}$, which is much lower than the recommended upper intake limit of zinc. The precipitation of phosphates on the skeleton surface is expected to enhance cell adherence and promote biocompatibility.

The formation of biofilm on the implants after surgical operation poses another challenge for metallic scaffolds. It has been demonstrated that iron has no antibacterial ability, and bacteria could easily form biofilm on its surface [53]. However, in the present study, nanometer-thick ZnO thin film enables porous iron scaffolds strong antibacterial ability against both Gram-positive and negative bacteria. Regarding to the antibacterial mechanism of ZnO, it is still in debate. Generally, four mechanisms have been proposed: (1) reactive oxygen species (ROS) mechanism [54–56], (2) zinc ions [57–59], (3) electrostatic interaction [60] and (4) membrane penetration [61, 62]. In this study, the zinc ions mechanism is more reasonable for the following factors: (1) The sustained release of a trace amount of Zn ions was observed in the immersion tests. (2) No ultraviolet radiation treatment on the scaffolds before antibacterial evaluation and the scaffolds with culture medium had never been exposed to visible light during the whole incubation period. Therefore, ROS has seldom chance to form. (3) The electrostatic interaction with bacterial cell membranes and membrane penetration mostly occurs when ZnO is in the form of nanoparticles. Zn ions could probably react with the membrane of bacteria resulting cell deformation and lysis [44, 63]. The sustained release of Zn ions could maintain the long-term antibacterial performance. Moreover, taking advantage of ALD, the thickness of ZnO films can be easily controlled by changing reaction cycles to meet the demand on different antibacterial period, which is significant to lower the risk of inflammation and inhibit biofilm formation during bone repair.

The in vitro cytotoxicity evaluation shows that ZnO@Fe scaffolds have certain cytotoxicity to MC3T3-E1 cells. It is found that the biocompatibility of Zn-based scaffolds in vitro is highly related to the concentration of Zn ions released in media that low concentration of Zn ions could increase the cell viability, proliferation, adhesion and osteogenic differentiation while high concentration exhibits strong cytotoxicity [52, 64–66]. The results in this work also confirm this concept, furthermore the diluting process indicates that with the help of dynamic substance exchange in local microenvironment in vivo, the cytotoxicity of ZnO@Fe scaffolds could be eliminated. For in vivo implants, mass exchange in biological bodies could accelerate the removal of excess Zn ions and corresponding degradation products in time; meanwhile, Zn ions could rapidly react with HPO_4^{2-} in surrounding microenvironment and produce zinc phosphates, which show high biocompatibility [44, 67]. Thus, a good performance would be expected when ZnO@Fe scaffolds are implanted in vivo.

5 Conclusion

In summary, we presented a facile and effective strategy to coat dense and uniform ZnO thin film on the 3D porous Fe

scaffolds with interconnected micropores. After coated with ZnO thin film, the degradation rate of the porous Fe scaffold was dramatically reduced. The ZnO@Fe scaffolds showed excellent antibacterial activity, with the antibacterial rate up to 87.0% and 88.4% against *E. coli* and *S. aureus*, respectively, without sacrificing the cytocompatibility. The antibacterial mechanism was probably attributed to the sustained release of Zn ions. The fabricated 3D porous ZnO@Fe with interconnected pores offers a promising antibacterial scaffold for bone repair and regeneration. Additionally, the present study also demonstrates that ALD is an effective method to coat thin films on the 3D porous scaffolds.

Acknowledgements This work was financially supported by the Natural Science Foundation of Guangdong (No. 2019A1515011755), China. The authors acknowledge the assistance of SUSTech Core Research Facilities that receives support from Presidential Fund and Development and Reform Commission of Shenzhen Municipality.

Declarations

Conflicts of interests The authors declare that they have no conflict of interests.

References

[1] Moravej M, Mantovani D. Biodegradable metals for cardiovascular stent application: interests and new opportunities. Int J Mol Sci. 2011;12(7):4250.
[2] Peuster M, Hesse C, Schloo T, Fink C, Beerbaum P, von Schnakenburg C. Long-term biocompatibility of a corrodible peripheral iron stent in the porcine descending aorta. Biomaterials. 2006;27(28):4955.
[3] Waksman R, Pakala R, Baffour R, Seabron R, Hellinga D, Tio FO. Short-term effects of biocorrodible iron stents in porcine coronary arteries. J Interv Cardiol. 2008;21(1):15.
[4] Peuster M, Wohlsein P, Brügmann M, Ehlerding M, Seidler K, Fink C, Brauer H, Fischer A, Hausdorf G. A novel approach to temporary stenting: degradable cardiovascular stents produced from corrodible metal—results 6–18 months after implantation into New Zealand white rabbits. Heart. 2001;86(5):563.
[5] Gorejová R, Haverová L, Oriňaková R, Oriňak A, Oriňak M. Recent advancements in Fe-based biodegradable materials for bone repair. J Mater Sci. 2019;54(3):1913.
[6] Alavi R, Trenggono A, Champagne S, Hermawan H. Investigation on mechanical behavior of biodegradable iron foams under different compression test conditions. Metals. 2017;7(6):202.
[7] Čapek J, Vojtěch D. Microstructural and mechanical characteristics of porous iron prepared by powder metallurgy. Mat Sci Eng C-Mater. 2014;43:494.
[8] Čapek J, Vojtěch D, Oborná A. Microstructural and mechanical properties of biodegradable iron foam prepared by powder metallurgy. Mater Des. 2015;83:468.
[9] He J, He FL, Li DW, Liu YL, Yin DC. A novel porous Fe/Fe-W alloy scaffold with a double-layer structured skeleton: preparation, in vitro degradability and biocompatibility. Colloid Surf B. 2016;142:325.
[10] Li Y, Jahr H, Lietaert K, Pavanram P, Yilmaz A, Fockaert LI, Leeflang MA, Pouran B, Gonzalez-Garcia Y, Weinans H, Mol JMC, Zhou J, Zadpoor AA. Additively manufactured biodegradable porous iron. Acta Biomater. 2018;77:380.
[11] Sharma P, Pandey PM. Corrosion behaviour of the porous iron scaffold in simulated body fluid for biodegradable implant application. Mat Sci Eng C-Mater. 2019;99:838.
[12] Wang X, Xu S, Zhou S, Xu W, Leary M, Choong P, Qian M, Brandt M, Xie YM. Topological design and additive manufacturing of porous metals for bone scaffolds and orthopaedic implants: a review. Biomaterials. 2016;83:127.
[13] Chou D-T, Wells D, Hong D, Lee B, Kuhn H, Kumta PN. Novel processing of iron–manganese alloy-based biomaterials by inkjet 3-D printing. Acta Biomater. 2013;9(10):8593.
[14] Heiden M, Nauman E, Stanciu L. Bioresorbable Fe–Mn and Fe–Mn–HA Materials for orthopedic implantation: enhancing degradation through porosity control. Adv Healthc Mater. 2017;6(13):1700120.
[15] Farack J, Wolf-Brandstetter C, Glorius S, Nies B, Standke G, Quadbeck P, Worch H, Scharnweber D. The effect of perfusion culture on proliferation and differentiation of human mesenchymal stem cells on biocorrodible bone replacement material. Mat Sci Eng B Adv. 2011;176(20):1767.
[16] Oriňák A, Oriňáková R, Králová Z, Turoňová A, Kupková M, Hrubovčáková M, Radoňák J, Džunda R. Sintered metallic foams for biodegradable bone replacement materials. J Porous Mater. 2014;21(2):131.
[17] Wang H, Zheng Y, Li Y, Jiang C. Improvement of in vitro corrosion and cytocompatibility of biodegradable Fe surface modified by Zn ion implantation. Appl Surf Sci. 2017;403:168.
[18] Su Y, Champagne S, Trenggono A, Tolouei R, Mantovani D, Hermawan H. Development and characterization of silver containing calcium phosphate coatings on pure iron foam intended for bone scaffold applications. Mater Des. 2018;148:124.
[19] He J, Ye H, Li Y, Fang J, Mei Q, Lu X, Ren F. Cancellous-bone-like porous iron scaffold coated with strontium incorporated octacalcium phosphate nanowhiskers for bone regeneration. ACS Biomater Sci Eng. 2019;5(2):509.
[20] Yang C, Huan Z, Wang X, Wu C, Chang J. 3D printed Fe scaffolds with HA nanocoating for bone regeneration. ACS Biomater Sci Eng. 2018;4(2):608.
[21] Ray S, Thormann U, Eichelroth M, Budak M, Biehl C, Rupp M, Sommer U, El Khassawna T, Alagboso FI, Kampschulte M, Rohnke M, Henß A, Peppler K, Linke V, Quadbeck P, Voigt A, Stenger F, Karl D, Schnettler R, Heiss C, Lips KS, Alt V. Strontium and bisphosphonate coated iron foam scaffolds for osteoporotic fracture defect healing. Biomaterials. 2018;157:1.
[22] Mohd Daud N, Sing NB, Yusop AH, Abdul Majid FA, Hermawan H. Degradation and in vitro cell–material interaction studies on hydroxyapatite-coated biodegradable porous iron for hard tissue scaffolds. J Orthop Transl. 2014;2(4):177.
[23] Yusop AHM, Daud NM, Nur H, Kadir MRA, Hermawan H. Controlling the degradation kinetics of porous iron by poly(lactic-co-glycolic acid) infiltration for use as temporary medical implants. Sci Rep. 2015;5:11194.
[24] Yusop AH, Sarian MN, Januddi FS, Ahmed QU, Kadir MR, Hartanto D, Hermawan H, Nur H. Structure, degradation, drug release and mechanical properties relationships of iron-based drug eluting scaffolds: the effects of PLGA. Mater Des. 2018;160:203.
[25] Wen Z, Zhang L, Chen C, Liu Y, Wu C, Dai C. A construction of novel iron-foam-based calcium phosphate/chitosan coating biodegradable scaffold material. Mat Sci Eng C Mater. 2013;33(3):1022.
[26] Gristina A. Biomaterial-centered infection: microbial adhesion versus tissue integration. Science. 1987;237(4822):1588.

[27] Hetrick EM, Schoenfisch MH. Reducing implant-related infections: active release strategies. Chem Soc Rev. 2006;35(9):780.
[28] Hardes J, Ahrens H, Gebert C, Streitbuerger A, Buerger H, Erren M, Gunsel A, Wedemeyer C, Saxler G, Winkelmann W, Gosheger G. Lack of toxicological side-effects in silver-coated megaprostheses in humans. Biomaterials. 2007;28(18):2869.
[29] Zhao L, Wang H, Huo K, Cui L, Zhang W, Ni H, Zhang Y, Wu Z, Chu PK. Antibacterial nano-structured titania coating incorporated with silver nanoparticles. Biomaterials. 2011;32(24):5706.
[30] Król A, Pomastowski P, Rafińska K, Railean-Plugaru V, Buszewski B. Zinc oxide nanoparticles: synthesis, antiseptic activity and toxicity mechanism. Adv Colloid Interface Sci. 2017;249:37.
[31] Jones N, Ray B, Ranjit KT, Manna AC. Antibacterial activity of ZnO nanoparticle suspensions on a broad spectrum of microorganisms. FEMS Microbiol Lett. 2008;279(1):71.
[32] Hameed ASH, Karthikeyan C, Ahamed AP, Thajuddin N, Alharbi NS, Alharbi SA, Ravi G. In vitro antibacterial activity of ZnO and Nd doped ZnO nanoparticles against ESBL producing Escherichia coli and Klebsiella pneumoniae. Sci Rep. 2016;6:24312.
[33] Zhang Y, Liu X, Li Z, Zhu S, Yuan X, Cui Z, Yang X, Chu PK, Wu S. Nano Ag/ZnO-incorporated hydroxyapatite composite coatings: highly effective infection prevention and excellent osteointegration. ACS Appl Mater Interface. 2018;10(1):1266.
[34] Mousa HM, Abdal-hay A, Bartnikowski M, Mohamed IMA, Yasin AS, Ivanovski S, Park CH, Kim CS. A multifunctional zinc oxide/poly(lactic acid) nanocomposite layer coated on magnesium alloys for controlled degradation and antibacterial function. ACS Biomater Sci Eng. 2018;4(6):2169.
[35] Alves MJ, Grenho L, Lopes C, Borges J, Vaz F, Vaz IP, Fernandes MH. Antibacterial effect and biocompatibility of a novel nanostructured ZnO-coated gutta-percha cone for improved endodontic treatment. Mat Sci Eng C Mater. 2018;92:840.
[36] Wang Z, Zhang L, Liu Z, Sang L, Yang L, Chen Q. The antibacterial polyamide 6-ZnO hierarchical nanofibers fabricated by atomic layer deposition and hydrothermal growth. Nanoscale Res Lett. 2017;12:421.
[37] Jin G, Qin H, Cao H, Qian S, Zhao Y, Peng X, Zhang X, Liu X, Chu PK. Synergistic effects of dual Zn/Ag ion implantation in osteogenic activity and antibacterial ability of titanium. Biomaterials. 2014;35(27):7699.
[38] Huo K, Zhang X, Wang H, Zhao L, Liu X, Chu PK. Osteogenic activity and antibacterial effects on titanium surfaces modified with Zn-incorporated nanotube arrays. Biomaterials. 2013;34(13):3467.
[39] Zhang P, Wu J, Zhang T, Wang Y, Liu D, Chen H, Ji L, Liu C, Ahmad W, Chen ZD, Li S. Perovskite solar cells with ZnO electron-transporting materials. Adv Mater. 2018;30(3):1703.
[40] Lin YY, Hsu CC, Tseng MH, Shyue JJ, Tsai FY. Stable and high-performance flexible ZnO thin-film transistors by atomic layer deposition. ACS Appl Mater Interface. 2015;7(40):22610.
[41] Chang E, Lee TM. Effect of surface chemistries and characteristics of Ti6Al4V on the Ca and P adsorption and ion dissolution in Hank's ethylene diamine tetra-acetic acid solution. Biomaterials. 2002;23(14):2917.
[42] Fosmire GJ. Zinc toxicity. Am J Clin Nutr. 1990;51(2):225.
[43] Shafaghi R, Rodriguez O, Wren AW, Chiu L, Schemitsch EH, Zalzal P, Waldman SD, Papini M, Towler MR. In vitro evaluation of novel titania-containing borate bioactive glass scaffolds. J Biomed Mater Res A. 2021;109(2):146.
[44] Su Y, Yang H, Gao J, Qin YX, Zheng Y, Zhu D. Interfacial zinc phosphate is the key to controlling biocompatibility of metallic zinc implants. Adv Sci. 2019;6(14):1900112.
[45] Li Y, Yan J, Zhou W, Xiong P, Wang P, Yuan W, Zheng Y, Cheng Y. In vitro degradation and biocompatibility evaluation of typical biodegradable metals (Mg/Zn/Fe) for the application of tracheobronchial stenosis. Bioact Mater. 2019;4:114.
[46] Trino LD, Albano LGS, Bronze-Uhle ES, George A, Mathew MT, Lisboa-Filho PN. Physicochemical, osteogenic and corrosion properties of bio-functionalized ZnO thin films: potential material for biomedical applications. Ceram Int. 2018;44(17):21004.
[47] Dong H, Zhou J, Virtanen S. Fabrication of ZnO nanotube layer on Zn and evaluation of corrosion behavior and bioactivity in view of biodegradable applications. Appl Surf Sci. 2019;494:259.
[48] Burke-Govey CP, Plank NOV. Review of hydrothermal ZnO nanowires: toward FET applications. J Vac Sci Technol B. 2013;31(6):06F101.
[49] Popescu MC, Ungureanu C, Buse E, Nastase F, Tucureanu V, Suchea M, Draga S, Popescu MA. Antibacterial efficiency of cellulose-based fibers covered with ZnO and Al_2O_3 by atomic layer deposition. Appl Surf Sci. 2019;481:1287.
[50] Cheng J, Huang T, Zheng YF. Microstructure, mechanical property, biodegradation behavior, and biocompatibility of biodegradable Fe–Fe_2O_3 composites. J Biomed Mater Res A. 2014;102(7):2277.
[51] Qiao Y, Zhang W, Tian P, Meng F, Zhu H, Jiang X, Liu X, Chu PK. Stimulation of bone growth following zinc incorporation into biomaterials. Biomaterials. 2014;35(25):6882.
[52] Cockerill I, Su Y, Sinha S, Qin YX, Zheng Y, Young ML, Zhu D. Porous zinc scaffolds for bone tissue engineering applications: a novel additive manufacturing and casting approach. Mat Sci Eng C Mater. 2020;110:110738.
[53] Ma Z, Gao M, Na D, Li Y, Tan L, Yang K. Study on a biodegradable antibacterial Fe-Mn-C-Cu alloy as urinary implant material. Mat Sci Eng C Mater. 2019;103:109718.
[54] Ghaemi B, Shaabani E, Najafi-Taher R, Jafari Nodooshan S, Sadeghpour A, Kharrazi S, Amani A. Intracellular ROS induction by Ag@ZnO core-shell nanoparticles: frontiers of permanent optically active holes in breast cancer theranostic. ACS Appl Mater Interface. 2018;10(29):24370.
[55] Aiswarya Devi S, Harshiny M, Udaykumar S, Gopinath P, Matheswaran M. Strategy of metal iron doping and green-mediated ZnO nanoparticles: dissolubility, antibacterial and cytotoxic traits. Toxicol Res. 2017;6(6):854.
[56] Kaviyarasu K, Maria Magdalane C, Kanimozhi K, Kennedy J, Siddhardha B, Subba Reddy E, Rotte NK, Sharma CS, Thema FT, Letsholathebe D, Mola GT, Maaza M. Elucidation of photocatalysis, photoluminescence and antibacterial studies of ZnO thin films by spin coating method. J Photoch Photobio B. 2017;173:466.
[57] Yang H, Zhang Q, Chen Y, He Y, Yang F, Lu Z. Microwave-ultrasonic synergistically assisted synthesis of ZnO coated cotton fabrics with an enhanced antibacterial activity and stability. ACS Appl Bio Mater. 2018;1:340.
[58] Li M, Zhu L, Lin D. Toxicity of ZnO nanoparticles to escherichia coli: mechanism and the influence of medium components. Environ Sci Technol. 2011;45(5):1977.
[59] Joe A, Park SH, Shim KD, Kim DJ, Jhee KH, Lee HW, Heo CH, Kim HM, Jang ES. Antibacterial mechanism of ZnO nanoparticles under dark conditions. J Ind Eng Chem. 2017;45:430.
[60] Nair S, Sasidharan A, Divya Rani VV, Menon D, Nair S, Manzoor K, Raina S. Role of size scale of ZnO nanoparticles and microparticles on toxicity toward bacteria and osteoblast cancer cells. J Mater Sci Mater Med. 2008;20:235.
[61] Zhong Q, Tian J, Liu T, Guo Z, Ding S, Li H. Preparation and antibacterial properties of carboxymethyl chitosan/ZnO

nanocomposite microspheres with enhanced biocompatibility. Mater Lett. 2018;212:58.
[62] Brayner R, Ferrari-Iliou R, Brivois N, Djediat S, Benedetti MF, Fiévet F. Toxicological impact studies based on *Escherichia coli* bacteria in ultrafine ZnO nanoparticles colloidal medium. Nano Lett. 2006;6(4):866.
[63] Sehgal RR, Carvalho E, Banerjee R. Mechanically stiff, zinc cross-linked nanocomposite scaffolds with improved osteostimulation and antibacterial properties. ACS Appl Mater Interface. 2016;8(22):13735.
[64] Zhang YK, Cui ZQ, Gong DQ, Wang WX, Cheng WL. Microstructure, fracture behavior, in vitro corrosion resistance, and cytotoxicity of Zn–Mg/Mg–Zn–HAp laminated composites produced by spark plasma sintering. Rare Met. 2021;40(4):939.
[65] Venezuela J, Dargusch MS. The influence of alloying and fabrication techniques on the mechanical properties, biodegradability and biocompatibility of zinc: a comprehensive review. Acta Biomater. 2019;87:1.
[66] He J, Fang J, Wei P, Li Y, Guo H, Mei Q, Ren F. Cancellous bone-like porous Fe@Zn scaffolds with core-shell-structured skeletons for biodegradable bone implants. Acta Biomater. 2021;121:665.
[67] Su Y, Wang K, Gao J, Yang Y, Qin YX, Zheng Y, Zhu D. Enhanced cytocompatibility and antibacterial property of zinc phosphate coating on biodegradable zinc materials. Acta Biomater. 2019;98:174.